

Original Article

Production of chitosan nanocomposite-dependent dual wound healing and its improved mechanism

Salhah D. Al-Qahtani, Ghadah M. Al-Senani*, Amal A. Al-Wallan

*Department of Chemistry, College of Science, Princess Nourah bint Abdulrahman University, Riyadh, Saudi Arabia

ARTICLE INFO

Keywords:
Antifungal activity
Chitosan nanocomposite
Wound healing

ABSTRACT

This study describes the preparation of novel chitosan-based nanoparticles loaded with *Boswellia serrata* extract (BSE-Cs NPs), with and without zinc oxide nanoparticles (ZnO NPs), via emulsification-solvent evaporation and nanoprecipitation. The obtained nanoformulations were characterized using dynamic light scattering (DLS), transmission electron microscopy (TEM), x-ray powder diffraction (XRD), and Fourier-transform infrared (FTIR) spectroscopy. XRD analysis confirmed the formation of a hexagonal wurtzite structure for the ZnO phase. The addition of ZnO NPs decreased the mean nanoparticle size from about 321 to 209 nm and changed the morphology to a more clustered structure, which suggests improved emulsification effectiveness. When compared to the conventional Amphotericin B antibiotic, the BSE-Cs/ZnO NP formulation had greater action against *Aspergillus niger*, exhibiting a strong, focused synergistic antifungal effect while maintaining constant antibacterial activity. In addition, the biocompatibility of the cytotoxic pure BSE was significantly enhanced by nano-encapsulation. For BSE-Cs NPs, the IC_{50} value rose from approximately 150 $\mu\text{g/mL}$ for pure BSE to over 1000 $\mu\text{g/mL}$. With an intermediate IC_{50} of about 700 $\mu\text{g/mL}$, the BSE-Cs/ZnO NP compound balanced ZnO's natural cytotoxicity with increased antifungal activity. A safe treatment window was indicated by the good biocompatibility of all formulations at lower doses. According to these results, BSE-Cs/ZnO NPs is a potential nanoformulation that provides a useful compromise between increased antifungal activity and tolerable cytotoxicity.

1. Introduction

The management of the wound healing process, particularly in cases of severe microbial infection, remains a significant burden in clinical practice [1,2]. The ideal wound dressing materials should not only provide a protective barrier against the external environment but also actively induce tissue regeneration and combat potential pathogens. With its advanced mechanisms for regulated medication administration and improved therapeutic results, the biomaterials field has been a groundbreaking discipline in recent years. Because of its remarkable biocompatibility, low toxicity, innate antibacterial and mucoadhesive qualities, and capacity to improve permeability and aid in hemostasis, chitosan (Cs) stands out among other biopolymers as a top contender for wound healing applications [3-5]. Chitosan-based polymeric nanoparticles (CsNPs) can be synthesized in a range of nanosizes (typically 10–1000 nm) using various methods [5-7], such as ionotropic gelation (the most common approach for CsNPs), emulsion solvent evaporation, the reverse micellar method, spray drying, and self-assembly (particularly for amphiphilic chitosan derivatives). Actually, the emulsification-solvent evaporation and nanoprecipitation techniques are among the most prevalent methods for encapsulating hydrophobic compounds—such as essential oils, poorly water-soluble

drugs (e.g., paclitaxel), and other lipophilic active agents—into polymer-based polymeric nanoparticles (PNPs) [8-10].

With their low toxicity, wide availability, natural biocompatibility, biodegradability, chemical inertness, and affordability, tree exudates are an extremely valuable class of natural biomaterials that provide a sustainable substitute for manufactured polymers. *Boswellia serrata* (family: *Burseraceae*), a tree indigenous to India's arid, hilly regions, is a classic example. Its exudate contains a substantial amount (~65%) of water-soluble polysaccharides, mainly arabinose, galactose, and xylose, in addition to strong bioactive boswellic acids [11]. The rich composition of *Boswellia serrata* gum resin, which is extracted by tapping the tree bark, is largely responsible for the plant's therapeutic potential. There are two main categories of bioactive substances in this resin [12]: (i) Boswellic acids are pentacyclic triterpenoid acids, including 3-O-acetyl-11-keto- β -boswellic acid (AKBA) and its direct precursor 11-keto- β -boswellic acid (KBA), which are the primary source of the potent anti-inflammatory feature. They function by controlling other immune response pathways, blocking important pro-inflammatory enzymes, particularly 5-lipoxygenase (5-LOX), and (ii) polysaccharides that make up a significant portion of the water-soluble fraction (~65%), these polysaccharides are primarily composed of arabinose, galactose, and xylose [13,14]. The *Boswellia serrata* resin (BSE) mucoadhesive qualities are enhanced by this composition, which makes it a great

*Corresponding author:

E-mail address: gmalsnany@pnu.edu.sa (G.M. Al-Senani)

Received: 17 November, 2025 Accepted: 05 March, 2026 Epub Ahead of Print: 04 May, 2026 Published: ***

DOI: 10.25259/AJC_1392_2025

option for drug delivery systems intended to stick to mucosal tissues or wound sites. Additionally, it is thought that these polysaccharides have wound-healing and immunomodulatory properties. Its distinctive makeup adds to its adaptable pharmacological profile, which makes it a strong contender for advancement in drug delivery and wound healing applications [15-17].

Indeed, ZnONPs are widely recognized for their diverse therapeutic qualities and are an essential part of inorganic nanomedicine [18-20]. They are useful biomaterials in the fight against infections because they have strong and wide spectrum antibacterial action against both Gram-positive and Gram-negative bacteria as well as unicellular and multicellular fungus [21-23]. They can release a variety of reactive oxygen species (ROS), including hydrogen peroxide (H_2O_2) and superoxide radicals (O_2^-), when exposed to light or moisture [23]. Microbial defense mechanisms are overpowered by this oxidative stress, which damages proteins, lipids, and DNA and ultimately results in cell death. ZnO NPs tiny size and positive surface charge make it easier for them to adhere to the negatively charged bacterial and fungal membranes. Because of this contact, the integrity of the membrane is compromised, enabling intracellular contents to seep out and perhaps allowing NPs to enter the cell and interfere with internal functions [24]. Furthermore, it has been demonstrated that ZnO NPs aid in wound healing by encouraging the migration of epithelial cells, improving tissue regeneration, and lowering inflammation [25,26]. They are a promising ingredient in sophisticated wound dressings, tissue engineering scaffolds, and antibacterial formulations due to their stability, ease of manufacture, and compatibility with biological systems [27,28].

This study tests a novel hypothesis that the synergistic integration of BSE, Cs, and ZnO NPs into a three-component nanocomposite will yield a functionally superior biomaterial for biomedical and other related applications. This approach aims to harness the specific roles of each component: Cs as a biocompatible carrier and permeation enhancer, BSE as a bioactive anti-inflammatory, and ZnO NPs for potent antimicrobial activity. The resulting composite is envisioned as a promising platform for advanced formulations, such as topical wound dressings or anti-acne therapies, where concurrent antimicrobial action and inflammation modulation are critical. The present work describes the synthesis of BSE and ZnO NP-loaded Cs nanoparticles (BSE-Cs/ZnONPs) using emulsification-solvent evaporation and nanoprecipitation techniques. The physicochemical characteristics, antibacterial activity against bacterial and fungal pathogens, cytotoxicity profile on human fibroblasts, and—most importantly—their capacity to promote *in vitro* wound healing were all carefully examined for the produced nanoformulations. We predict that this ternary nanocomposite will demonstrate a synergistic effect, providing an exceptional balance between strong targeted antimicrobial actions, markedly decreased cytotoxicity, and accelerated wound closure, thereby offering a very promising platform for advanced wound care management.

2. Materials and Methods

Boswellia serrata resin (Yemeni/Omani Frankincense) was purchased from local supplier SA. Cs with low molecular weight (50–190 kDa, deacetylation degree $\geq 75\%$) was purchased from Sigma-Aldrich, USA. ZnO NPs (zinc oxide nanopowder, <50 nm particle size (BET), purity >97%) were purchased from Sigma-Aldrich, USA. Zinc acetate dihydrate salt ($Zn(CH_3COO)_2 \cdot 2H_2O$, $\geq 99.5\%$ purity, product of EMSURE®) was obtained from Sigma-Aldrich, USA. Glacial acetic acid and ethanol (analytical grade) were purchased from Fisher Scientific (Loughborough, U.K.).

2.1. *Boswellia serrata* resin (BSE) extraction process

Prior to extraction, the *Boswellia serrata* was grinded and sieved using a 250 μm sieve. Briefly, finely powdered resin (50 g) was dispersed in 250 ml of 96% methanol solution. The mixture was then kept under slow stirring at 40°C for 24 h in the dark condition before filtration using Whatman grade 50 filter paper. To assess the extraction yield (%), ethanol was evaporated under reduced pressure at 40°C.

The Oleo-gum-resin (BSE) was collected and stored at 4°C for further studies.

2.2. Chitosan-loaded BSE and ZnO nanoparticles by emulsification and nanoprecipitation methods

BSE-loaded Cs nanoparticles (BSE-CsNPs) were produced as follows [9]: Cs solution was prepared by dissolving 1 g of Cs powder in 100 mL deionized water containing 0.5 ml glacial acetic acid using a magnetic stirrer for 30 min. After that, 0.5 g of BSE was dissolved in 5 ml chloroform solution and added slowly to the Cs solution under vigorous stirring. The mixture was then homogenized using the homogenizer at approximately 6,000 rpm for 15 min. The obtained emulsion was kept under magnetic stirring at 200 rpm for 3 h to evaporate the organic solvent. Then, the BSE-CsNPs were precipitated using 10 mL of sodium hydroxide solution (0.5 M). Finally, the NPs were collected and washed by three centrifugation cycles at 6,000 rpm for 4 min, discarding the supernatant and re-suspending the nanoparticle pellets in deionized water, and then lyophilized for 24 h to obtain BSE-CsNPs nanopowders.

To prepare the composite BSE-CsNPs/ZnONPs, 1.25 g of zinc acetate salt was dissolved in 100 mL of Cs/BSE solution and stirred at room temperature. After 2 h, about 3 ml of 1 M sodium hydroxide aqueous solution was added slowly to the Zn/Cs/BSE mixture till reaching pH~9. The obtained whitish precipitate was kept under vigorous stirring at 40°C for 2 h. The mixture was also centrifuged at 6,000 rpm for 5 min. The supernatant was removed, and the BSE-Cs/ZnONPs pellets were lyophilized for 24 h.

2.3. Microstructure characterization

The size and shape of the as-prepared BSE-CsNPs and BSE-Cs/ZnONPs were observed by transmission electron microscopy (TEM) (JEOLH-7650, Hitachi High-Technologies Corp., Tokyo, Japan). The size distribution, mean particle size, and zeta potential for BSE-CsNPs and BSE-Cs/ZnONPs were determined by the dynamic light scattering device (DLS: Malvern Zetasizer Nano ZS Instruments Ltd, UK). Fourier transform infrared spectroscopy (FTIR) of all samples was done by Jasco, FTIR-6100 type A, Japan. The FTIR spectra are obtained in the region 4000 – 400 cm^{-1} . Phase analysis of the as-prepared nanoparticles is applied using x-ray diffractometer (XRD) Bruker D8 advance CuK target with a secondary monochromator at 40 kV and 40mA.

2.4. Antimicrobial activity

The antimicrobial efficacy of the resultant nanoparticles was evaluated against a panel of standard pathogenic strains, including the Gram-positive bacterium (i.e. *Staphylococcus aureus*), the Gram-negative bacterium (i.e. *Escherichia coli*), the unicellular fungal yeast (i.e. *Candida albican*), and the multicellular filamentous fungus (i.e. *Aspergillus niger*). Prior to testing, bacterial strains were pre-activated by inoculation in Nutrient Broth medium for 24 h at 37°C. To encourage activation and reach a high spore density (about 10 CFU/mL), fungal strains were pre-cultured in potato dextrose broth (PDB) for 48 h at 28°C while being shaken. Initially, the turbidimetric approach was used in Mueller Hinton Broth (MHB) to screen each drug at a fixed concentration of 100 $\mu g/mL$. Using the agar diffusion method, antimicrobial activity was further evaluated on solid medium: microbial suspensions were added to MHB plates, and the inhibition zone diameter (in millimeters) was measured following incubation [29]. All tested compounds were compared to standard antibacterial and antifungal agents. For compounds showing notable activity, the minimum inhibitory concentration (MIC) was done according to Clinical and Laboratory Standards Institute (CLSI) guidelines [30]. Results were quantified using colony-forming unit (CFU) counts to confirm inhibitory effects.

2.5. Fibroblast cell isolation and cell culture

Human fibroblast cells were isolated from nasal mucosa tissue [31]. The isolation protocol was performed as follows: Tissue samples were dissected into approximately 3 × 1 mm pieces with a disposable scalpel. To ensure sterility, the tissue pieces were sequentially washed in 70% ethanol, Sterillium® classic pure (Bode Chemie GmbH, Germany), and

70% ethanol again. The sterilized tissue was then transferred into 5–10 mL of 0.5% protease solution (P6141, Sigma-Aldrich, St. Louis, MO, USA) in phosphate buffered saline (PBS) and incubated overnight at 4°C. The following day, the protease solution was shaken for 15 min at 37°C. The digested tissue was filtered through a 70 μm EASYstrainer™ (Greiner Bio-One, Austria), and cells were released using a cell scraper (Falcon®, Corning, NY, USA). After centrifugation at 1,500 rpm for 4 min, the cell pellet was resuspended in cell culture medium and seeded into 25 cm² culture flasks. The fibroblast cells were kept in DMEM/Ham's F12 medium (ThermoFisher Scientific, USA) supplemented with 10% fetal calf serum and antibiotics (penicillin 10,000 U/mL and streptomycin 10 mg/mL; Sigma-Aldrich, USA) at 37°C in a 5% CO₂ atmosphere. Fibroblasts were observed morphologically and used within passage 10 to preserve primary cell characteristics.

2.6. Cellular viability

To assess cytotoxicity, cells were seeded in a 96-well plate at a density of 10,000 cells per well in 250 μL of complete culture medium and allowed to adhere for 24 h. Following adhesion, the medium was replaced with serum-free (FCS-free) medium containing either BSE-Cs NPs or BSE-Cs/ZnONPs at specified concentrations; serum-free medium alone served as the untreated control. After a 48 h incubation time, the treatment medium was carefully removed and replaced with fresh serum-free medium containing 10% AlamarBlue™ Cell Viability Reagent (ThermoFisher Scientific, USA) [32]. Cells were incubated with the reagent for 4 h at 37°C. The fluorescence was then measured using a Fluoroskan Ascent Microplate Fluorometer (ThermoFisher Scientific, USA) with an excitation wavelength of 538 nm and an emission wavelength of 600 nm. The viability results are shown as relative fluorescence units, normalized to the untreated control cells.

2.7. Wound healing assay (Migration assay)

To evaluate cellular migratory capability, a standardized wound healing (scratch) assay was performed by using culture inserts placed in a 35 mm $\mu\text{-Dish}$ (ibidi® GmbH, Germany). Briefly, 20,000 cells were seeded into each chamber of the insert in 80 μL of cell culture medium and allowed to adhere overnight. After 24 h, the insert was carefully removed, creating a defined cell-free gap. The cells were then treated with the specified concentrations of BSE-Cs NPs or BSE-Cs/ZnONPs, suspended in serum-free (FCS-free) medium; serum-free medium alone served as the untreated control. The wound closure was monitored over time by capturing images of the same scratch region at regular intervals

from 24 to 240 h post-treatment. To ensure objective and quantitative analysis of cell migration, the gap closure was evaluated using the automated “T-Scratch” software (cse-lab.ethz.ch/software.html).

2.8. Statistical analysis

All data are presented as the mean and standard deviation ($\pm\text{SD}$). Statistical comparisons of cell viability and migration assays were performed using one-way or two-way ANOVA, as appropriate. The research experiments were accomplished at the Natural and Health Sciences Research Center. The significance threshold: $p < 0.05$ (marked with * $p < 0.05$). The research experiments were accomplished at the Natural and Health Sciences Research Center.

3. Results and Discussion

In this study, the emulsification-solvent evaporation and nanoprecipitation methods were used to encapsulate BSE within Cs nanoparticles and the subsequent incorporation of ZnONPs. The obtained nanoparticle size distribution was measured using TEM and DLS methods, which are the most popular and common techniques for determining the size distribution profile of nanoformulated suspension (Figure 1). The physicochemical parameters of the obtained nanoformulations (Table 1) showed that both CS-BSE NPs and BSE-Cs/ZnO NPs had a broad size distribution and nanosize diameters. As shown in Figures 1(a and c), the CS-BSE NPs sample exhibits a regular spherical morphology with an average size of 321 ± 90 nm, while BSE-Cs/ZnO NPs sample appears smaller with a more clustered structure, having an average size of 209 ± 53 nm. The size reduction suggests that the addition of ZnO nanoparticles (ZnONPs) to the BSE-Cs suspension changed the formulation, probably by improving emulsification efficiency (e.g., decreased BSE droplet coalescence) and lowering interfacial tension during solvent evaporation, according to the TEM data. As shown in Table 1 and Figure 1(b) and 1(d), the DLS measurement showed that the size distribution was a single population

Table 1. Represents TEM and DLS measurements for determining the size distribution profile of the obtained nanoformulation.

Sample name	Zeta potential (mV)	DLS size distribution \pm SD (nm)	PDI	TEM particles mean size (nm)
BSE-Cs NPs	11.1 \pm 4.5	277.7 \pm 32.7	0.85	321 \pm 90
BSE-Cs/ZnONPs	-21.1 \pm 3.9	663. \pm 148 (20%) 139 \pm 30 (80%)	0.79	209 \pm 53

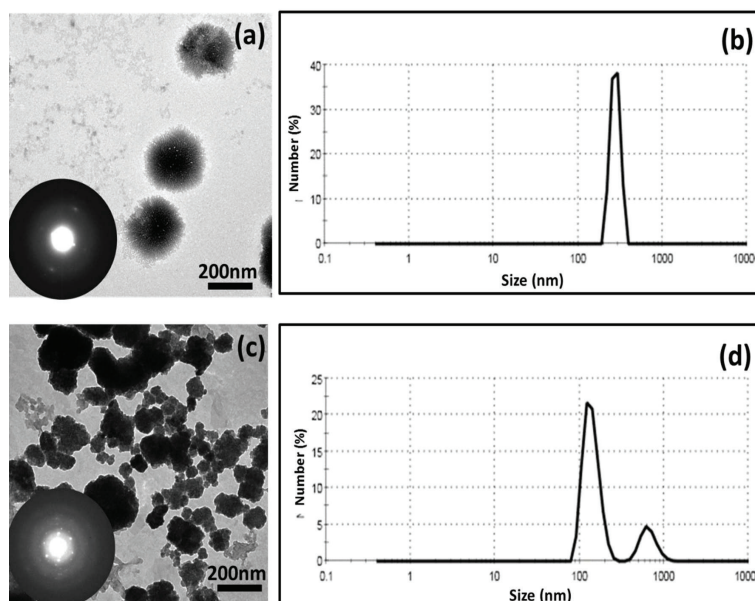


Figure 1. (a,b) TEM micrographs and DLS analysis of BSE-Cs NPs; (c,d) TEM micrographs and DLS analysis of BSE-Cs/ZnO NPs.

of 277.7 ± 32.7 nm diameter and 11.1 ± 4.5 mV zeta potential value for BSE-Cs NPs and a biomodel population of 663 ± 148 (20%) 139 ± 30 (80%) with a zeta potential -21.1 ± 3.9 mV for BSE-Cs/ZnONPs. In the context of TEM results, the magnitude of size reduction in the main population was nearly 50%, decreasing from 277 nm to 139 nm. This confirms the role of ZnO NPs in enhancing emulsification efficiency and solvent evaporation. Furthermore, zeta potential (-21.1 mV) is borderline stable (typically $|\zeta| > 30$ mV is needed for strong electrostatic repulsion) and explains why 20% aggregates persist despite the net-negative charge. It is important to mention that the TEM-DLS size mismatch (TEM (321 nm) > DLS (278 nm)), which is unusual since DLS typically reports larger hydrodynamic diameters, could be attributed to the extreme polydispersity values (PDI: 0.79-0.85), pointing to severe aggregation that manifest differently across techniques.

Figure 2 presents the FTIR spectroscopy analysis of neat Cs, pure BSE extract, BSE-loaded Cs nanoparticles (BSE-CsNPs), and the zinc oxide nanocomposite (BSE-Cs/ZnONPs). The spectra were analyzed to confirm the successful formation of the nanoparticles and to identify key molecular interactions between the components. The spectrum of pure Cs exhibits its characteristic bands primarily: O-H and N-H stretches at 3357 cm^{-1} (from hydroxyl and amine groups), C-H stretches at around $2982\text{-}2863 \text{ cm}^{-1}$ (from the pyranose ring), amide groups at 1653 cm^{-1} (remaining from the original chitin structure), N-H bend at 1589 cm^{-1} (primary amine, $-\text{NH}_2$), asymmetric stretching of the C-O-C bridge at 1142 cm^{-1} (characteristic of the glycosidic linkage between sugar units) and C-O stretch at 1071 and 1034 cm^{-1} (primary and secondary hydroxyl, C-OH). For neat BSE, the broad peak around $3400\text{-}3200 \text{ cm}^{-1}$ is assigned to O-H stretching vibration. This is a hallmark of hydroxyl groups ($-\text{OH}$). In *Boswellia serrata*, this primarily comes from the carboxylic acid ($-\text{COOH}$) group of boswellic acids (especially AKBA, etc.) and possibly from traces of water or other alcohols/phenols. The peaks around 2932 cm^{-1} and 2853 cm^{-1} are related to C-H stretching vibrations. These peaks are from methyl ($-\text{CH}_3$) and methylene ($-\text{CH}_2-$) groups. They are abundant in the complex ring structures (pentacyclic triterpenoid skeleton) of boswellic acids and other terpenes in the resin. The strong peak around 1707 cm^{-1} is due to C=O stretching vibration, which is one of the most important peaks for identifying *Boswellia serrata*. It is characteristic of the carbonyl group (C=O) of a carboxylic acid ($-\text{COOH}$), which is a key functional group in boswellic acids. The exact position can shift slightly depending on the specific boswellic acid and hydrogen bonding. The other peaks at 1452 cm^{-1} and 1367 cm^{-1} , 1234 cm^{-1} , 1027 cm^{-1} are assigned to C-H bending (scissoring and symmetric bending), C-O bonds, and C-O-C stretch. For the BSE-Cs sample: The amide and amine peaks were shifted to a lower wavenumber (e.g., to $1640\text{-}1559 \text{ cm}^{-1}$) and changed in intensity. This is a classic sign of the

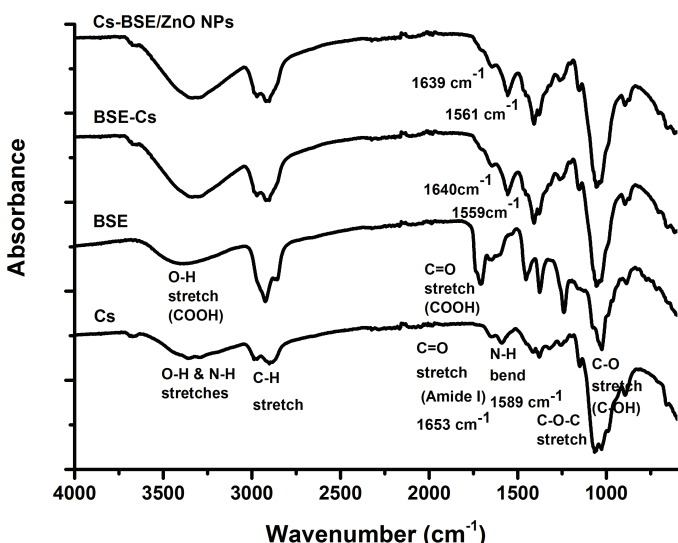


Figure 2. FTIR spectra of Cs, BSE, BSE-CsNPs and BSE-Cs/ZnONPs samples.

protonation of the amine group ($-\text{NH}_2 \rightarrow -\text{NH}_3^+$). The boswellic acids in BSE (e.g., β -boswellic acid, AKBA) are organic acids. They can donate a proton (H^+) to chitosan's amine group, forming a chitosan-boswellate salt complex. In addition, there was a change in the broadening of the O-H/N-H stretch peak at around $3400\text{-}3200 \text{ cm}^{-1}$. The observed shifts and broadening of peaks confirm a molecular interaction, most likely an ionic bond and hydrogen bonding, between the boswellic acids in the *Boswellia serrata* extract and the Cs polymer. This interaction is crucial for the stability and formation of nanoparticles (CsNPs) loaded with the extract. However, the fact that the spectrum of BSE-Cs/ZnONPs closely resembles that of BSE-Cs (with no distinct new Zn-O peak) suggests the following scenarios: The primary interaction is still between BSE and Cs. ZnONPs are physically encapsulated within or surrounded by the dense organic matrix of the BSE-Cs complex. The characteristic Zn-O stretching vibration ($\sim 400\text{-}600 \text{ cm}^{-1}$) is a relatively weak absorber compared to the strong organic functional group vibrations (C=O, O-H, N-H). This is very common in polymer/ceramic nanocomposites where the polymer phase dominates the FTIR signal.

The XRD patterns of neat Cs, pure BSE, ZnONPs (Sigma-Aldrich), and the ZnO nanocomposite (BSE-Cs/ZnONPs) are demonstrated in Figure 3. The sigma ZnONPs showed a perfect match for the hexagonal wurtzite structure of ZnO (JCPDS No. 36-1451) with distinct diffraction peaks at 2θ values $\sim 31.8^\circ(100)$, $\sim 34.4^\circ(002)$, $\sim 36.3^\circ(101)$, $\sim 47.5^\circ(102)$, $\sim 56.6^\circ(110)$, $\sim 62.9^\circ(103)$, $\sim 66.4^\circ(200)$, $\sim 68.0^\circ(112)$, $\sim 69.1^\circ(201)$. The XRD pattern for pure Cs exhibits two main characteristic diffraction peaks at 2θ values around 10.6° and 20.3° . These peaks are attributed to the crystal structure of chitosan. The XRD graph of the crude boswellia serrate powder showed a pattern with broad, low-intensity humps instead of sharp peaks at 2θ value of 15.4° , indicating a predominantly amorphous structure. On the other side, the BSE-Cs/ZnONPs sample showed very sharp, intense, and narrow peaks at $31.5^\circ(100)$, $34.9^\circ(002)$, $36.1^\circ(101)$, $48.7^\circ(102)$, $57.2^\circ(110)$, $61.3^\circ(103)$, $68.2^\circ(112)$, confirming the presence of crystalline ZnO nanoparticles. The broad characteristic humps of Cs at $2\theta \sim 20^\circ$ and BSE (at $2\theta \sim 15^\circ$) were not observed in the BSE-Cs/ZnONPs sample. This indicates a disruption of chitosan's ordered domains due to the interaction between ZnO nanoparticles and the functional groups ($-\text{NH}_2$, $-\text{OH}$) of Cs breaks up the hydrogen-bonded network, making the polymer matrix more amorphous [33,34].

3.1. Antimicrobial activity

The antimicrobial test showed that the largest zones of inhibition were observed against *S. aureus* and *A. niger*. The BSE sample consistently exhibits moderate antibacterial activity. However, as Table 2 and Figure 4 demonstrate, the Cs-BSE NPs sample antibacterial

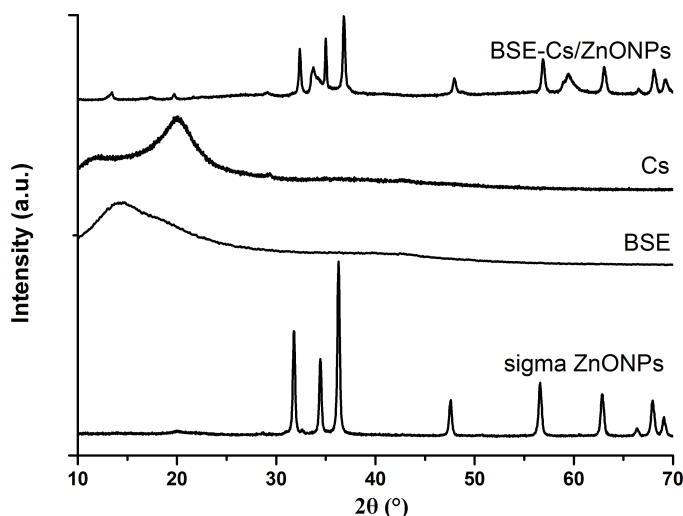


Figure 3. XRD pattern of Cs, ZnONPs, BSE, BSE-Cs/ZnONPs.

Table 2. Antimicrobial activity of the prepared samples using agar well diffusion method.

Sample code	Inhibition zone (mm)			
	<i>Staphylococcus aureus</i>	<i>Escherichia coli</i>	<i>Candida albicans</i>	<i>Aspergillus niger</i>
BSE	3	2	3	ND
BSE-CsNPs	4	3	3	3
BSE-Cs/ ZnONPs	2	2	3	5
Polymyxin B	3	2	-	-
Amphotericin B	-	-	5	4

Polymyxin B was used as standard antibacterial agents, while Amphotericin B was used as standard antifungal agents at 20 µg/mL.

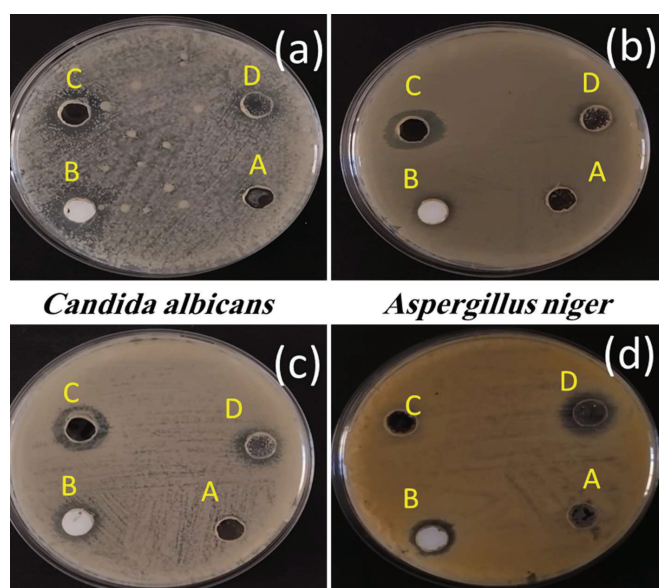


Figure 4. The antimicrobial test against different pathogens using agar well diffusion method: (a) *Escherichia coli*, (b) *Staphylococcus aureus*, (c) *Candida albicans*, and (d) *Aspergillus niger*. The samples are labeled as follows: (A) Control water, (B) BSE-CsNPs, (C) BSE, and (D) BSE-Cs/ZnONPs.

activity is marginally higher than that of the pure extract. This implies boswellic acids and Cs work in concert. The bacterial cell membrane is probably disrupted by Cs, a recognized antibacterial polymer [35], but boswellic acids, with their pentacyclic triterpenoid structure, may disturb cellular processes and increase activity [36]. The antibacterial activity of Cs/BSA/ZnONPs is surprisingly lower (2 mm each) than that of the Cs/BSE and BSE-NPs samples. According to XRD/FTIR results, the ZnO nanoparticles may be deeply incorporated into the Cs-BSE matrix, "locking them up" and limiting their capacity to contact bacteria. Conversely, every sample exhibits a comparable zone of inhibition (~3 mm) against *C. albicans*. The most significant finding is the activity of BSE-Cs/ZnONPs formulation against *A. niger*, with a zone of inhibition (5 mm) that is larger than the standard antifungal Amphotericin B (4 mm) at the tested concentration. This is a powerful indicator of a strong synergistic antifungal effect specifically against *A. niger* that only occurs when chitosan, boswellic acid, and zinc oxide are combined.

MIC (µg/mL) is the lowest concentration of a given substance that inhibits visible growth of a microorganism. A lower MIC value indicates a more potent antimicrobial compound against that specific microbe. The test nanoparticles (BSE-CsNPs, and BSE-Cs/ZnONPs) were compared to the standard antibiotics and BSE, as shown in Table 3. The Cs-BSE-NPs sample demonstrates strong and specific activity against the yeast *C. albicans*, matching their potency against *S. aureus*. This makes them a promising candidate for anti-fungal applications. The BSE-Cs/ZnONPs sample shows interesting properties. While it was

Table 3. Minimum inhibitory concentration (MIC) of the prepared nanoformulation.

Sample name	Minimum inhibitory concentration (MIC, µl/mL)			
	<i>Staphylococcus aureus</i>	<i>Escherichia coli</i>	<i>Candida albicans</i>	<i>Aspergillus niger</i>
BSE NPs	240	240	240	< 300
Cs-BSANPs	120	240	120	80
Cs-BSA/ ZnONPs	80	240	80	80
Polymyxin B	31.5	7.5	-	-
Amphotericin B	-	-	20	10

the least effective against bacteria and fungi, it was one of the most effective against the mold *Aspergillus niger*. This suggests a possible synergistic effect where the combination of chitosan/BSE with ZnO creates a formulation particularly potent against molds [23]. All novel nanoparticles showed significantly lower activity against *E. coli* compared to the standard drug. This is common as the outer membrane of Gram-negative bacteria is a formidable barrier, and overcoming it is a key challenge in antimicrobial development.

The activity of the prepared formulations can be better understood by comparing the inhibition zone and MIC data. The BSE-Cs/ZnONPs composite demonstrated narrow zones of inhibition against bacteria (2 mm), but it extremely low MIC of 80 µg/mL against *S. aureus* confirms strong bactericidal activity, indicating that direct-contact assays more accurately reflect the efficacy of the nanoparticle than diffusion-based test [23,37]. On the other hand, this formulation exceeded the usual Amphotericin B and demonstrated a strong and specific antifungal synergy against *A. niger*, resulting in the biggest inhibitory zone (5 mm) and a low MIC (80 µg/mL). A broad-spectrum synergistic interaction of Cs and boswellic acids was confirmed by the Cs/BSE-NPs consistent, improved activity in both assays, with broader zones and lower MIC values than the pure extract [35]. These findings demonstrate that the BSE-Cs/ZnONPs composite has focused, potent antibacterial activity, especially against fungal pathogens, which may be inaccurate by diffusion-based techniques alone.

3.2. Cell viability and wound healing assays

To assess the effect of pure BSE and chitosan-based formulation on cellular viability and cytotoxicity of human fibroblasts, the Alamar Blue bioassay has been utilized in this study as shown in Figure 5. The conducted analysis has shown that the pure BSE extract is highly cytotoxic to human fibroblasts at concentrations above 50 µg/mL. This is a known phenomenon and aligns with the literature showing that boswellic acids can induce cell death at high doses [36]. The IC₅₀ for pure BSE sample was around ~150 µg/mL. While the BSE-CsNPs nanoformulations showed high viability even at higher doses, which indicates better biocompatibility. The IC₅₀ for BSE-CsNPs sample was more than 1000 µg/mL. Since Cs is known to be biocompatible, it serves as a barrier to protect the boswellic acids, which probably makes it easier for them to release gradually and under control. This enables the cells to withstand considerably higher total concentrations by preventing an abrupt, hazardous release of the drug into the cells. On the other hand, BSE-Cs/ZnONPs sample shows an intermediate toxicity profile. Its IC₅₀ is lower than BSE-CsNPs but still higher than pure BSE, estimated to be between 400 and 1000 µg/mL (~700 µg/mL). The increased toxicity compared to BSE-CsNPs is almost certainly due to the added cytotoxic effect of ZnO nanoparticles on the fibroblasts, which is a well-documented effect. It is also important to mention that all samples at low concentrations (10 & 50 µg/mL) including the pure BSE, show excellent biocompatibility with cell viability at or near 100%. In addition, a critical divergence begins at intermediate concentrations (100 & 200 µg/mL). The cytotoxicity of the pure BSE becomes apparent.

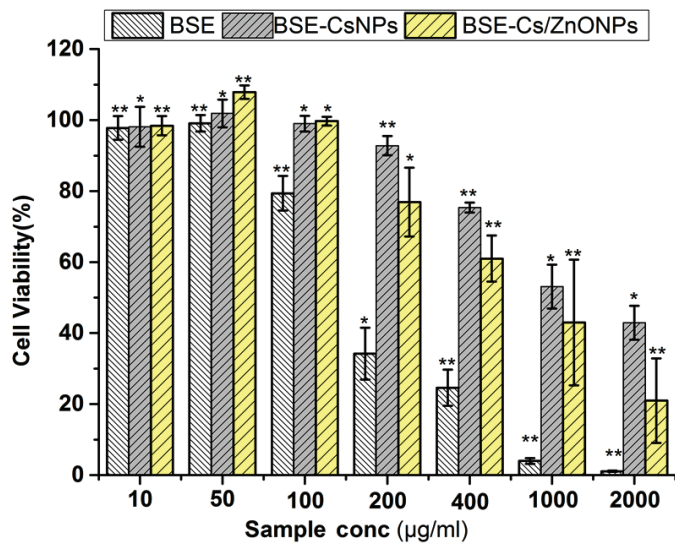


Figure 5. Cellular viability of fibroblasts treated with concentrations of pure BSE and chitosan-based formulation ranging from 10 µg/ml to 2000 µg/ml using the alamar blue bioassay. * means significant difference ($p < 0.05$) and ** means high significant difference ($p > 0.05$) compared to control.

The viability drops to ~79% at 100 µg/mL and plummets to ~34% at 200 µg/mL. The nano-formulations (BSE-Cs/ZnONPs & BSE-CsNPs) continue to show high biocompatibility. Viability remains above 92% at 200 µg/mL for BSE-CsNPs and above 76% for BSE-Cs/ZnONPs.: The difference is dramatic at high concentrations (400 - 2000 µg/mL). The pure BSE is highly toxic, almost completely killing the cells (< 5% viability) at 1000 µg/mL and above. The nanoformulations show a significantly slower decline in viability. The chitosan-only nanoparticles (BSE-CsNPs) perform best, protecting cells and maintaining >42% viability even at 2000 µg/mL. The ZnO-containing composite (BSE-Cs/ZnONPs) is more toxic than CsNPs but still far less toxic than pure BSE.

The *in vitro* fibroblast wound healing assay was structured with multiple variables: time points (24h/48h/72h), treatment types (BSE, BSE-CsNPs, BSE-Cs/ZnONPs), and concentrations (10/50/100 µg/ml plus control). The wound closure percentage values are shown in Figure 6. The wound closure percentages for control (untreated cells) were 21.4% closure at 72 h compared to ~77-96% for the treated groups. This baseline confirms that all treatments significantly enhance the wound healing process compared to natural cell migration/proliferation alone. Indeed, the BSE-Cs/ZnONPs composite consistently showed the best or among the best wound closure rates, especially at the critical early stage (24 h) and 50 µg/ml dose. All three treatments at a dose perform (10 µg/ml) are very similar at all points of time. The differences are within the margin of error (shown by the standard deviation ±). Further increasing the treatment dose, the BSE-Cs/ZnONPs (48%) and BSE-CsNPs (52%) show dramatically better closure than plain BSE (35.6%). This indicates

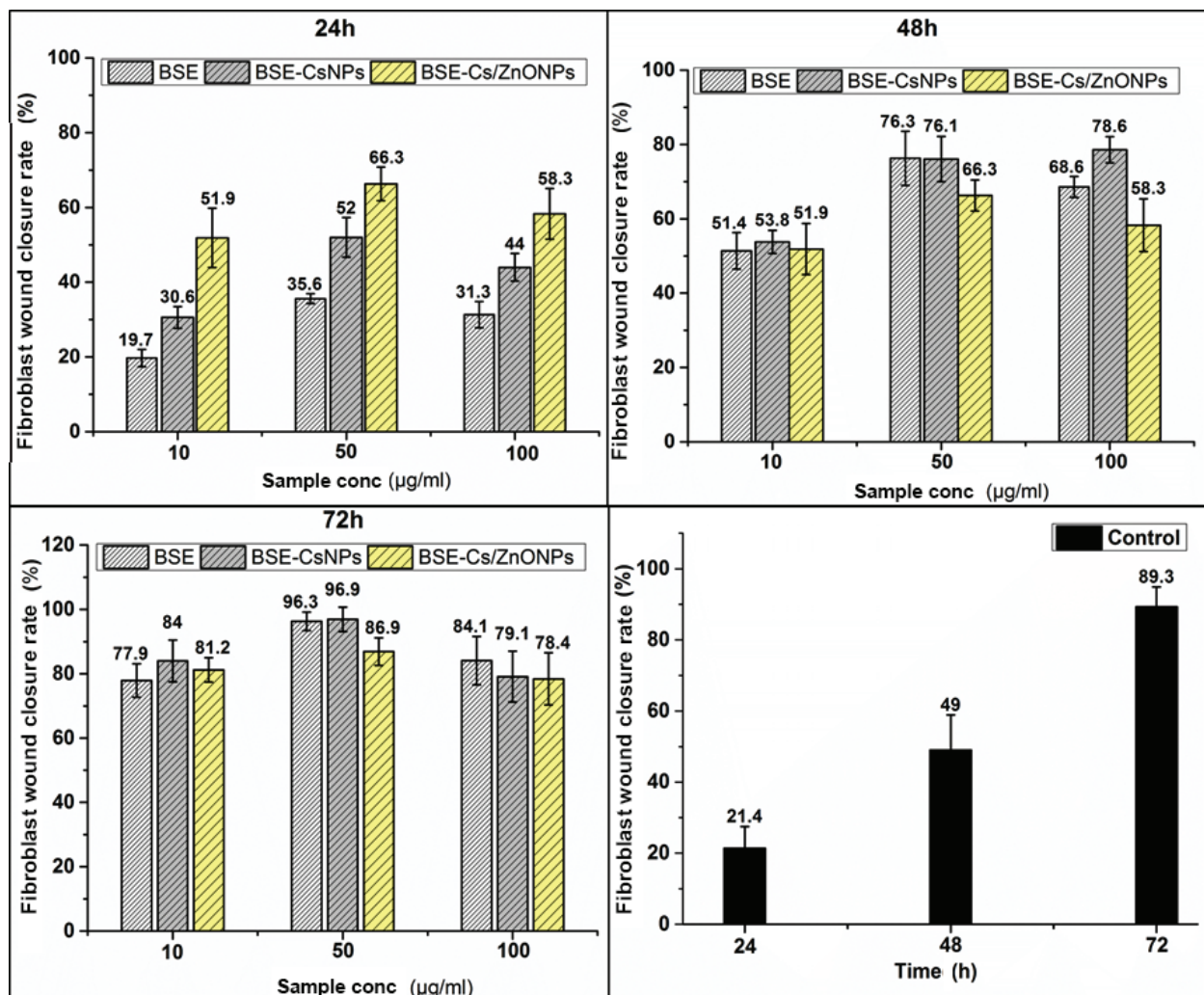


Figure 6. Shows the percentage of wound closure at three different time points (24, 48, and 72 h) for three different treatments at various concentrations (10, 50, 100 µg/ml), plus a control group with no treatment.

a much faster initiation of the healing process. Interestingly, the healing potential drops at a dose of 100 µg/ml compared to the 50 µg/ml dose for the formulation groups (BSE-Cs/ZnONPs and BSE-CsNPs), while plain BSE improves slightly.

4. Conclusions

This study successfully developed and characterized novel BSE-Cs and BSE-Cs/ZnONPs. The physicochemical characterizations (TEM, DLS, XRD, FTIR) indicate that the incorporation of ZnONPs fundamentally altered the properties of the BSE-Cs formulation, significantly reducing particle size and creating a composite nanostructure. This integration also resulted in a targeted and powerful synergistic effect, in which the BSE-Cs/ZnO NP formulation demonstrated superior, specific antifungal activity against *A. niger*. This suggests a unique antimicrobial mechanism that is only unlocked by the combination of all three components. Furthermore, the BSE-Cs formulation dramatically mitigated the inherent cytotoxicity of neat BSE, significantly widening its therapeutic window. While the addition of ZnONPs introduced a degree of cytotoxicity compared to the BSE-CsNPs, the composite nanoformulation (BSE-Cs/ZnO NP) still represented a substantial improvement over neat BSE. Therefore, even though BSE-Cs/ZnONPs appears to be a very promising antifungal platform, to fully evaluate its translational potential, future work must prioritize validation against a wide panel of clinical and drug-resistant isolates, mechanistic studies using methods like XPS and ROS assays, and the assessment of long-term stability and *in vivo* performance.

CRedit authorship contribution statement

Salhah D. Al-Qahtani: Conceptualization, Methodology, Visualization, Investigation, Supervision, Data curation, Software, Validation, Writing-Original draft preparation, Writing-Reviewing and Editing. **Ghadah M. Al-Senani:** Methodology, Visualization, Investigation, Software, Validation, Writing-Reviewing and Editing. **Amal A. Al-Wallan:** Investigation, Supervision, Data curation, Software, Writing- Original draft preparation.

Declaration of competing interest

There are no conflicts of interest.

Data availability

The data that support the findings of this study are available from the corresponding author upon reasonable request.

Declaration of generative AI and AI-assisted technologies in the writing process

The authors confirm that there was no use of artificial intelligence (AI)-assisted technology for assisting in the writing or editing of the manuscript and no images were manipulated using AI.

Acknowledgment

This research was funded by the Deanship of Scientific Research and Libraries at Princess Nourah bint Abdulrahman University, through the "Nafea" Program, Grant No. (NP-45-022).

References

- Cristea Hohotă, A.G., Lisă, E.L., Iacob Ciobotaru, S., Dragostin, I., Ştefan, C.S., Fulga, I., Anghel Ştefan, A.M., Dragan, M., Morariu, I.D., Dragostin, O.M., 2025. Antimicrobial smart dressings for combating antibiotic resistance in wound care. *Pharmaceuticals (Basel, Switzerland)*, **18**, 825. <https://doi.org/10.3390/ph18060825>
- Malone, M., Schultz, G., 2022. Challenges in the diagnosis and management of wound infection. *The British Journal of Dermatology*, **187**, 159-166. <https://doi.org/10.1111/bjd.21612>
- Nagpal, K., Singh, S.K., Mishra, D.N., 2010. Chitosan nanoparticles: A promising system in novel drug delivery. *Chemical & Pharmaceutical Bulletin*, **58**, 1423-1430. <https://doi.org/10.1248/cpb.58.1423>
- Bashir, S.M., Ahmed Rather, G., Patricio, A., Haq, Z., Sheikh, A.A., Shah, M.Z.U.H., Singh, H., Khan, A.A., Imtiyaz, S., Ahmad, S.B., Nabi, S., Rakhshan, R., Hassan, S., Fonte, P., 2022. Chitosan nanoparticles: A versatile platform for biomedical applications. *Materials (Basel, Switzerland)*, **15**, 6521. <https://doi.org/10.3390/ma15196521>
- Divya, K., Jisha, M.S., 2018. Chitosan nanoparticles preparation and applications. *Environmental Chemistry Letters*, **16**, 101-112. <https://doi.org/10.1007/s10311-017-0670-y>
- Grenha, A., 2012. Chitosan nanoparticles: A survey of preparation methods. *Journal of Drug Targeting*, **20**, 291-300. <https://doi.org/10.3109/1061186X.2011.654121>
- Rampino, A., Borgogna, M., Blasi, P., Bellich, B., Cesàro, A., 2013. Chitosan nanoparticles: Preparation, size evolution and stability. *International Journal of Pharmaceutics*, **455**, 219-228. <https://doi.org/10.1016/j.ijpharm.2013.07.034>
- Chaudhary, S.A., Patel, D.M., Patel, J.K., Patel, D.H. (2021). Solvent emulsification evaporation and solvent emulsification diffusion techniques for nanoparticles. In: *Emerging technologies for nanoparticle manufacturing*. 287-300. (Cham: Springer international publishing). https://doi.org/10.1007/978-3-030-50703-9_12
- Hernández-Giottonini, K.Y., Rodríguez-Córdova, R.J., Gutiérrez-Valenzuela, C.A., Peñuñuri-Miranda, O., Zavala-Rivera, P., Guerrero-Germán, P., Lucero-Acuña, A., 2020. PLGA nanoparticle preparations by emulsification and nanoprecipitation techniques: Effects of formulation parameters. *RSC Advances*, **10**, 4218-4231. <https://doi.org/10.1039/c9ra10857b>
- Alshamsan, A., 2014. Nanoprecipitation is more efficient than emulsion solvent evaporation method to encapsulate cucurbitacin I in PLGA nanoparticles. *Saudi Pharmaceutical Journal: SPJ: The Official Publication of the Saudi Pharmaceutical Society*, **22**, 219-222. <https://doi.org/10.1016/j.jsps.2013.12.002>
- Al-Harrasi, A., Khan, A. L., Asaf, S., & Al-Rawahi, A. (2019). Taxonomy, distribution and ecology of *Boswellia*. In biology of genus *Boswellia* (pp. 11-34). Cham: Springer International Publishing. <https://doi.org/10.1007/978-3-030-16725-7>
- Ammon, H.P., 2016. Boswellic acids and their role in chronic inflammatory diseases. *Advances in Experimental Medicine and Biology*, **928**, 291-327. https://doi.org/10.1007/978-3-319-41334-1_13
- Herrmann, A., König, S., Lechtenberg, M., Sehlbach, M., Vakhrushev, S.Y., Peter-Katalinic, J., Hensel, A., 2012. Proteoglycans from *Boswellia serrata roxb.* and *B. carteri Birdw.* and identification of a proteolytic plant basic secretory protein. *Glycobiology*, **22**, 1424-1439. <https://doi.org/10.1093/glycob/cws107>
- Sharma, S., Thawani, V., Hingorani, L., Shrivastava, M., Bhatte, V. R., & Khiyani, R. (2004). Pharmacokinetic study of 11-keto β-Boswellic acid. *Phytomedicine*, **11** (2-3), 255-260. <https://doi.org/10.1078/0944-7113-00290>
- Abdel-Tawab, M., Werz, O., Schubert-Zsilavec, M., 2011. *Boswellia serrata*: An overall assessment of *in vitro*, preclinical, pharmacokinetic and clinical data. *Clinical Pharmacokinetics*, **50**, 349-369. <https://doi.org/10.2165/11586800-000000000-00000>
- Hasson, S.O., Jasim, A.M., Salman, S.A.K., Akrami, S., Saki, M., Hassan, M.A., 2022. Evaluation of antibacterial and wound-healing activities of alcoholic extract of *Boswellia carterii*, *in vitro* and *in vivo* study, **21**, 6199-6208. <https://doi.org/10.1111/jocd.15206>
- Pengzong, Z., Yuanmin, L., Xiaoming, X., Shang, D., Wei, X., Zhigang, L., Dongzhou, D., Wenjing, Y., Jianbiao, Y., Yang, X., Xia, L., 2019. Wound healing potential of the standardized extract of *Boswellia serrata* on experimental diabetic foot ulcer via inhibition of inflammatory, angiogenic and apoptotic markers. *Planta Medica*, **85**, 657-669. <https://doi.org/10.1055/a-0881-3000>
- Islam, F., Shohag, S., Uddin, M.J., Islam, M.R., Nafady, M.H., Akter, A., Mitra, S., Roy, A., Emran, T.B., Cavalu, S., 2022. Exploring the journey of zinc oxide nanoparticles (ZnO-NPs) toward biomedical applications. *Materials (Basel, Switzerland)*, **15**, 2160. <https://doi.org/10.3390/ma15062160>
- Anjum, S., Hashim, M., Malik, S.A., Khan, M., Lorenzo, J.M., Abbasi, B.H., Hano, C., 2021. Recent advances in zinc oxide nanoparticles (ZnO NPs) for cancer diagnosis, target drug delivery, and treatment. *Cancers*, **13**, 4570. <https://doi.org/10.3390/cancers13184570>
- Kumar, B., Smita, K., Cumbal, L., Debut, A., 2014. Green approach for fabrication and applications of zinc oxide nanoparticles. *Bioinorganic Chemistry and Applications*, **2014**, 523869. <https://doi.org/10.1155/2014/523869>
- Mirzaei, H., Darroudi, M., 2017. Zinc oxide nanoparticles: Biological synthesis and biomedical applications. *Ceramics International*, **43**, 907-914. <https://doi.org/10.1016/j.ceramint.2016.10.051>
- Lallo da Silva, B., Abuçafy, M.P., Berbel Manaia, E., Oshiro Junior, J.A., Chiari-Andréo, B.G., Pietro, R.C.R., Chiavacci, L.A., 2019. Relationship between structure

- and antimicrobial activity of zinc oxide nanoparticles: An overview. *International Journal of Nanomedicine*, **14**, 9395-9410. <https://doi.org/10.2147/IJN.S216204>
23. Sirelkhatim, A., Mahmud, S., Seeni, A., Kaus, N.H.M., Ann, L.C., Bakhori, S.K.M., Hasan, H., Mohamad, D., 2015. Review on zinc oxide nanoparticles: antibacterial activity and toxicity mechanism. *Nano-Micro Letters*, **7**, 219-242. <https://doi.org/10.1007/s40820-015-0040-x>
24. Palanikumar, L., Ramasamy, S.N., Balachandran, C., 2014. Size-dependent antimicrobial response of zinc oxide nanoparticles. *IET Nanobiotechnology*, **8**, 111-117. <https://doi.org/10.1049/iet-nbt.2012.0008>
25. Pino, P., Bosco, F., Molle, C., Onida, B., 2023. Antimicrobial Nano-zinc oxide biocomposites for wound healing applications: A review. *Pharmaceutics*, **15**, 970. <https://doi.org/10.3390/pharmaceutics15030970>
26. Raguvaran, R., Manuja, B.K., Chopra, M., Thakur, R., Anand, T., Kalia, A., Manuja, A., 2017. Sodium alginate and gum acacia hydrogels of ZnO nanoparticles show wound healing effect on fibroblast cells. *International Journal of Biological Macromolecules*, **96**, 185-191. <https://doi.org/10.1016/j.ijbiomac.2016.12.009>
27. Pérez-Díaz, M.A., Prado-Prone, G., Díaz-Ballesteros, A., González-Torres, M., Silva-Bermudez, P., Sánchez-Sánchez, R., 2023. Nanoparticle and nanomaterial involvement during the wound healing process: An update in the field. *Journal of Nanoparticle Research*, **25**. <https://doi.org/10.1007/s11051-023-05675-9>
28. Laurenti, M., Cauda, V., 2017. ZnO nanostructures for tissue engineering applications. *Nanomaterials (Basel, Switzerland)*, **7**, 374. <https://doi.org/10.3390/nano7110374>
29. Mishra, A., Sharma, A. K., Kumar, S., Saxena, A. K., & Pandey, A. K. (2013). *Bauhinia variegata* leaf extracts exhibit considerable antibacterial, antioxidant, and anticancer activities. *BioMed Research International*, 915436. <https://doi.org/10.1155/2013/915436>
30. Silva-Santana, G., da Conceição, G.M.S., Brandão, M.L.L., Mattos-Guaraldi, A.L., Júnior, R.H., 2025. Standardized method for quantifying colony-forming units in *Corynebacterium striatum* and *Staphylococcus aureus* biofilms on hydrophilic and hydrophobic surfaces. *Journal of Microbiological Methods*, **237**, 107216. <https://doi.org/10.1016/j.mimet.2025.107216>
31. Hussain, R., Hugosson, S., Roomans, G.M., 2014. Isolation and culture of primary human nasal epithelial cells from anesthetized nasal epithelia. *Acta Oto-Laryngologica*, **134**, 296-299. <https://doi.org/10.3109/00016489.2013.859396>
32. Xu, M., McCanna, D.J., Sivak, J.G., 2015. Use of the viability reagent prestoblue in comparison with alamarblue and MTT to assess the viability of human corneal epithelial cells. *Journal of Pharmacological and Toxicological Methods*, **71**, 1-7. <https://doi.org/10.1016/j.vascn.2014.11.003>
33. Hezma, A.M., Rajeh, A., Mannaa, M.A., 2019. An insight into the effect of zinc oxide nanoparticles on the structural, thermal, mechanical properties and antimicrobial activity of Cs/PVA composite. *Colloids and Surfaces A: Physicochemical and Engineering Aspects*, **581**, 123821. <https://doi.org/10.1016/j.colsurfa.2019.123821>
34. Prokhorov, E., Luna-Bárcenas, G., Yáñez Limón, J.M., Gómez Sánchez, A., Kovalenko, Y., 2020. Chitosan-ZnO nanocomposites assessed by dielectric, mechanical, and piezoelectric properties. *Polymers*, **12**, 1991. <https://doi.org/10.3390/polym12091991>
35. Raafat, D., Sahl, H.G., 2009. Chitosan and its antimicrobial potential – a critical literature survey. *Microbial Biotechnology*, **2**, 186-201. <https://doi.org/10.1111/j.1751-7915.2008.00080.x>
36. Liu, J.J., Nilsson, A., Oredsson, S., Badmaev, V., Zhao, W.Z., Duan, R.D., 2002. Boswellic acids trigger apoptosis via a pathway dependent on caspase-8 activation but independent on Fas/Fas ligand interaction in colon cancer HT-29 cells. *Carcinogenesis*, **23**, 2087-2093. <https://doi.org/10.1093/carcin/23.12.2087>
37. Balouiri, M., Sadiki, M., Ibsouda, S.K., 2016. Methods for *in vitro* evaluating antimicrobial activity: A review. *Journal of Pharmaceutical Analysis*, **6**, 71-79. <https://doi.org/10.1016/j.jpha.2015.11.005>